ORNL/TM-9239

ornl

OAK RIDGE NATIONAL LABORATORY

MARTIN MARIETTA

The Calculation of Stellarator Equilibria in Vacuum Flux Surface Coordinates

T. C. Hender
B. A. Carreras
L. Garcia
J. A. Rome
V. E. Lynch

OPERATED BY
MARTIN MARIETTA ENERGY SYSTEMS, INC.
FOR THE UNITED STATES
DEPARTMENT OF ENERGY

ORNL/TM-9239
Dist. Category UC-20

FUSION ENERGY DIVISION

THE CALCULATION OF STELLARATOR EQUILIBRIA IN VACUUM FLUX SURFACE COORDINATES

T. C. Hender, B. A. Carreras, L. Garcia, J. A. Rome
Fusion Energy Division

V. E. Lynch
Computer Sciences

Date Published - September 1984

Prepared by
OAK RIDGE NATIONAL LABORATORY
Oak Ridge, Tennessee 37831
operated by
MARTIN MARIETTA ENERGY SYSTEMS, INC.
for the
U.S. DEPARTMENT OF ENERGY
under Contract No. DE-AC05-84OR21400

CONTENTS

ABSTRACT

Details are given of a three-dimensional stellarator equilibrium code NEAR. This code uses a set of vacuum flux coordinates as an Eulerian basis for the equilibrium calculations. This coordinate system provides an economic representation of the complex geometry associated with stellarators. The equilibrium equations are solved by an energy minimization technique employing a conjugate gradient iteration scheme. The results of extensive numerical convergence studies are presented. Also comparisons with existing codes are made to benchmark the NEAR code.

1. INTRODUCTION

The study of magnetohydrodynamic (MHD) equilibria in stellarator configurations is greatly complicated by the fully three-dimensional (3-D) nature of the device. Several approximations may be introduced that permit analytic or semi-analytic equilibrium solutions. The method of averaging, in which the vacuum helical magnetic field is treated as a rapidly fluctuating small scale perturbation to the dominant toroidal field, reduces the stellarator equilibrium problem to a two-dimensional (2-D) problem [1]. An alternate analytic approach has been to make an expansion about the magnetic axis [2].

To study stellarator equilibria without ordering expansions generally requires the use of numerical methods. Most of the numerical approaches use a variational technique to solve for the equilibria. The Chodura-Schlüter code [3] solves the equilibrium equations by minimising the energy on a cylindrical coordinate Eulerian grid. The Bauer, Betancourt and Garabedian code[4] solves the so-called inverse equilibrium problem, in which the equilibrium problem is reformulated into that of solving for the flux coordinates, instead of solving directly for magnetic fields and pressure.

In this paper, the NEAR code, which solves the 3-D equilibrium problem directly by an energy minimization technique, will be described. The NEAR code formulation is similar to that of the Chodura-Schlüter code except that a vacuum flux coordinate system is employed as the Eulerian frame of reference for the calculation. An Eulerian formulation is chosen because it allows the study of equilibria whose flux surface topology changes with pressure. The vacuum flux coordinates (ρ,θ,ϕ) are obtained numerically from the

vacuum magnetic fields specified by a given coil configuration. The metric elements and Jacobian of the flux coordinates are represented by Fourier series in the generalized poloidal (θ) and toroidal (ϕ) angles of the flux coordinates. Details of the vacuum flux coordinates will be given in Section 2. The dependent variables in the equilibrium computation are also represented as Fourier series in θ, ϕ. In the radial direction (ρ), a finite difference representation is used. Using the vacuum flux coordinates in this manner, as an Eulerian basis, will be shown to provide a far more efficient description of geometrically complicated stellarator equilibria than the spatial coordinate finite difference representation used in Chodura-Schlüter code. This permits a much finer spatial numerical resolution to be achieved. The equilibrium equations and their solution by the NEAR code algorithm will be described in Section 3. To illustrate the numerical properties of NEAR, equilibrium results will be shown in Section 4, for the Advanced Toroidal Facility (ATF) configuration [5], and for a 12-field period heliac [6]. For the ATF equilibria, comparisons will be made with other computations. Finally, in Section 5, conclusions will be given.

2. VACUUM FLUX COORDINATES

The flux coordinate system employed is that described by Boozer [7]. For a vacuum, the magnetic field may be described in contravariant form as

$$\vec{B}_v = B_0 \rho \, \vec{\nabla}\rho \times \vec{\nabla}(\theta - \iota\phi) \tag{1}$$

or in covariant form as

$$\vec{B}_v = F_v \, \vec{\nabla}\phi \quad , \tag{2}$$

where $\iota(\rho)$ is the rotational transform, F_v is a constant, and $B_0\rho^2/2 = \psi_T$ is the toroidal flux. The role of a radial variable is taken by ρ. The potential ϕ may be regarded as a toroidal variable and for appropriate choice of the constant F_v, ϕ changes by 2π in traversing the torus once toroidally. Finally, the role of a poloidal angle is taken by θ, which changes by 2π in going once around the torus poloidally.

These coordinates are generated numerically in a manner described by Kuo-Petravic et al., using the method and code described in Ref. [8]. This code generates the Fourier series representation of the cylindrical coordinates (R,Z,ζ) in the vacuum flux coordinates θ and ϕ by following vacuum magnetic field lines. The particular coil configurations, whose equilibria have been studied, are composed of a series of identical field periods or modules. Also, within each field period a symmetry exists; at equal toroidal angle distances from either end of the field period, the R coordinates of the coils will be the same, while the Z coordinates will be equal and opposite. This

symmetry means that for an appropriate choice of flux coordinate origin, the Fourier representation of R contains only cosine terms and those of Z and $(\zeta - \phi)$, only sine terms. Thus, for example

$$R(\rho,\theta,\phi) = \sum_{m,n} R_{m,n}(\rho) \cos(m\theta + n\phi) \ , \qquad (3)$$

where n is restricted to multiples of the number of field periods (including n = 0). In practice, of course, only a finite number of terms may be retained in these Fourier series descriptions. Figure 1 shows how error in representing the vacuum quantities R, Z, and $|\vec{B}|$ depends on the number of terms in the Fourier series. Here the error is defined as

$$\underset{-\pi<\theta,\phi<\pi}{\text{Max}} \left(\frac{\left| \sum_{m,n} A_{m,n} \cos(m\theta + n\phi) - A(\theta,\phi) \right|}{|A(\theta,\phi)|} \right) ;$$

that is, the maximum difference between the true value and the value from the Fourier series with a given number of terms, normalized to the true value. The particular case illustrated in Fig. 1 is for the planar axis ATF device. The order in which the $A_{m,n}$ are included in the Fourier series is chosen to optimize its convergence. At 7 harmonics the modes retained are $(m = 0 \rightarrow 2,\ n = 0)$ and $(m = -3 \rightarrow 0,\ n = 12)$, and at 17 harmonics the modes are $(m = 0 \rightarrow 4,\ n = 0)$, $(m = -5 \rightarrow 2,\ n = 12)$ and $(m = -3 \rightarrow -1,\ n = 24)$. It can be seen that the Fourier representation provides an economic and rapidly convergent description of the vacuum fields. Typically between 10 and 20 harmonics are used to describe the vacuum quantities in the equilibrium calculation. Helical axis configurations, however, generally have a

broader Fourier spectra and may require more harmonics to adequately represent the vacuum fields.

Using the Fourier representations of R, Z, and ζ, the metric elements may be computed. In practice, to obtain a quasi-cylindrical-like set of coordinates with the normal axis behavior, the coordinates used are $(\rho,(\rho\theta),\phi)$. Thus, for example, the Jacobian is

$$D_v = \vec{\nabla}\rho \times \vec{\nabla}(\rho\theta) \cdot \vec{\nabla}\phi = \frac{|\vec{B}_v|^2}{B_0 F_v}, \tag{4}$$

and

$$g_{\theta\theta} = \frac{1}{\rho^2}\left[\left(\frac{\partial R}{\partial \theta}\right)^2 + R^2\left(\frac{\partial \zeta}{\partial \theta}\right)^2 + \left(\frac{\partial Z}{\partial \theta}\right)^2\right]. \tag{5}$$

For simplicity, the super and subscript θ is used for the $(\rho\theta)$ component. Various interrelationships show that the only independent metric elements which must be computed are $g_{\rho\rho}$, $g_{\rho\theta}$, and $g_{\theta\theta}$.

Having solved the equilibrium problem in these flux coordinates, it is desirable to be able to view the solutions in real space. This may easily be achieved using the R, Z, and ζ transformations [e.g., Eq. (3)]. In particular, the magnetic surfaces are computed by following magnetic field lines in the vacuum flux coordinates and recording the points at which they puncture given constant toroidal angle (ζ) planes. The coordinates of these punctures are then transformed to real space coordinates and the magnetic surfaces are plotted. This procedure is more accurate than transforming to real space and then following magnetic field lines; particularly since (as

explained in the next section) $\vec{\nabla} \cdot \vec{B} = 0$ is maintained to the accuracy of the finite difference approximations throughout the equilibrium calculation in the vacuum flux coordinates.

3. EQUILIBRIUM EQUATIONS AND NUMERICS

(a) Equilibrium Equations

The approach to solving the equilibrium problem is the same as that of the Chodura-Schlüter code [3]. A fictitious force $\vec{F}$ is introduced

$$\vec{F} = (\vec{\nabla} \times \vec{B}) \times \vec{B} - \vec{\nabla}P \ . \tag{6}$$

This force is related to a velocity using a conjugate gradient iteration scheme

$$\vec{V}^{n+1} = \vec{F}^{n+1} + \alpha \frac{\langle \vec{F}^2 \rangle^{n+1}}{\langle \vec{F}^2 \rangle^{n}} \vec{V}^{n} \ , \tag{7}$$

where superscripts denote iteration level, angled brackets denote a volume average, and α is a constant. For optimal convergence α is chosen just less than unity [3]. Using this velocity, the magnetic field $\vec{B}$, is advanced in a flux conserving manner,

$$\frac{\partial \vec{B}}{\partial t} = \vec{\nabla} \times (\vec{V} \times \vec{B}) \ . \tag{8}$$

The pressure P, which is related to the density by the adiabatic pressure law, is advanced in a mass conserving manner,

$$\frac{\partial P}{\partial t} = -\vec{V} \cdot \vec{\nabla} P - \gamma P \nabla \cdot \vec{V} , \tag{9}$$

where γ is the ratio of specific heats. From Eqs. (6), (8), and (9), the rate of change of potential energy is

$$\frac{dW}{dt} \equiv \frac{d}{dt} \int (P/(\gamma - 1) + B^2/2) d\tau = -\int \vec{V} \cdot \vec{F} \, d\tau . \tag{10}$$

Thus, if $\vec{V} \cdot \vec{F}$ is positive definite, the potential energy will always decrease and the final steady state will be an equilibrium $[\vec{\nabla} P = \vec{J} \times \vec{B}]$. The obvious choice for the iteration scheme is the friction model $\vec{V} = \vec{F}$; however, the conjugate gradient method [Eq. (7)] gives a far more rapid convergence.

(b) Numerical Algorithm and Differencing

In the numerical implementation of the above equations [Eqs. (6) through (9)] the dependent variables are V^ρ, V^θ, V^ϕ, (B^θ/D_v), (B^ϕ/D_v), and P. The main reason for time advancing $(\vec{B}/D_v)$ instead of $\vec{B}$ is that in the flux coordinates $\vec{V} \cdot \vec{B} = 0$ is

$$\frac{1}{\rho} \frac{\partial}{\partial \rho} \left(\rho \frac{B^\rho}{D_v} \right) + \frac{1}{\rho} \frac{\partial}{\partial \theta} \left(\frac{B^\theta}{D_v} \right) + \frac{\partial}{\partial \phi} \left(\frac{B^\phi}{D_v} \right) = 0 . \tag{11}$$

Thus (B^ρ/D_v) may be computed from Eq. (11), once (B^θ/D_v) and (B^ϕ/D_v) have been time advanced. This procedure maintains the important

physical property that $\vec{\nabla} \cdot \vec{B} = 0$, throughout the calculation, and is also more efficient than time advancing (B^ρ/D_v) directly.

The numerical algorithm used in the NEAR code is summarized in the flow diagram shown in Fig. 2. The dependent variables are represented in finite difference form in the radial direction (ρ). The variables V^ρ and (B^ρ/D_v) are discretized on a uniformly spaced ρ-mesh, whose first point is the coordinate axis ($\rho = 0$) and whose last point is at the wall. The remaining variables [V^θ, V^ϕ, (B^θ/D_v), (B^ϕ/D_v), and P] are on an intermediate mesh whose points lie halfway between those of the V^ρ, (B^ρ/D_v) mesh. Centered finite differences are used to approximate the ρ derivatives. In an earlier version of the NEAR code, all the dependent variables were represented on the same radial mesh. This, however, led to grid separation problems arising from the hyperbolic nature of the equations — the highest derivatives that are present are first order, which only effectively couple every other grid point and thus permit grid separation. By using the two distinct grids as previously described, these grid separation problems are overcome.

Since the metric elements are represented as Fourier series in θ and ϕ it is natural to also represent the dependent variables in this manner. The symmetry arising from the coils which was discussed in Section 2 means that (B^ρ/D_v), V^θ, V^ϕ can be represented by sine series and (B^θ/D_v), (B^ϕ/D_v), V^ρ, and P can be represented by cosine series. Thus, for example,

$$V^\rho(\rho,\theta,\phi,t) = \sum_{m,n} V^\rho_{m,n}(j,t) \cos(m\theta + n\phi) \quad . \tag{12}$$

This Fourier representation requires that the convolutions of Fourier series be calculated numerically. These convolutions are performed

numerically using the simple trigonometric formulae for the products of sines and cosines. Fast Fourier transforms are not used to compute these convolutions. The choice of the (m,n) spectrum used in the calculations will be discussed in the next section. Simple first order explicit differencing is used in time. The finite difference form of the equations solved is given in the appendix.

(c) Boundary and Initial Conditions

The magnetic field is initialized to its numerically obtained vacuum value:

$$\frac{B^{\rho}}{D_v} = 0 \ ,$$

$$\frac{B^{\theta}}{D_v} = B_0 \varkappa \rho \ , \tag{13}$$

$$\frac{B^{\phi}}{D_v} = B_0 \ .$$

The velocity is initialized to zero, and the initial pressure (P_I) is assumed to be of the form

$$P_I = a(1 - \rho^2)^m \ , \tag{14}$$

where a and m are constants [for all the results presented in this paper, m = 2]. In the code, analytic forms are used for the radial derivatives of the initial pressure (P_I) occurring in Eqs. (8) and (9).

The boundary conditions are those of an infinitely conducting wall at the last closed vacuum flux surface. The boundary conditions on the radial velocity and magnetic field are

$$V^{\rho}\big|_{wall} = \left(\frac{B^{\rho}}{D_v}\right)\Big|_{wall} = 0 \ . \tag{15}$$

The remaining dependent variables are on the intermediate mesh and their values are never required at the wall. At the coordinate axis ($\rho = 0$) regularity imposes certain constraints on the behavior of the dependent variables. In particular, the (m,n) component of V^{ρ}, V^{θ}, (B^{ρ}/D_v), (B^{θ}/D_v) must go to zero at least as fast as $\rho^{||m|-1|}$ and V^{ϕ}, (B^{ϕ}/D_v), P must go to zero at least as fast as $\rho^{|m|}$. The additional constraints that

$$V^{\rho}_{m,n} = -m\, V^{\theta}_{m,n}$$

and (16)

$$\left(\frac{B^{\rho}}{D_v}\right)_{m,n} = m\left(\frac{B^{\theta}}{D_v}\right)_{m,n}$$

must also be satisfied by the $m = 1$ components at $\rho = 0$. For the dependent variables (B^{θ}/D_v), (B^{ϕ}/D_v), V^{ϕ}, P an additional mesh point is included at $\rho = 0$. The variables V^{ρ}, V^{ϕ}, (B^{θ}/D_v), (B^{ϕ}/D_v), and P are advanced in time at the origin, using one-sided approximations to the radial derivatives, and values of the $m = 1$ components of V^{θ} and (B^{ρ}/D_v) are determined using Eqs. (16).

4. COMPUTATIONAL RESULTS

In this section, the numerical properties of the NEAR code will be investigated by studying equilibria for the planar axis ATF and for a 12-field period heliac. For each new configuration studied the convergence properties must be examined. The results given here for the heliac and ATF are fairly representative of machines of their class. The ATF device, in its standard mode of operation, is a 12-field period $\ell = 2$ torsatron with a rotational transform (ι) varying between ~0.3 at the magnetic axis and ~1.0 at the plasma edge.

There are several parameters for which numerical convergence studies must be made. First the selection of (m,n) mode pairs to be included in the equilibrium calculations will be considered. As a general rule, the importance of a mode in the vacuum representation gives a good guide to the importance of that mode in the equilibrium calculation. This is because a large harmonic in the metric elements and Jacobian leads to good couplings to that particular harmonic during the evolution to an equilibrium. Figure 3 shows the dominant harmonics of $|B|^2$ as function of ρ for the ATF vacuum. The (1,0) harmonic is associated with the toroidicity, while the (-2,12) harmonic is due to the helical coils. The (-1,12) and (-3,12) harmonics are the toroidal side-bands of the (-2,12) harmonic. Figure 4 shows the spectrum of energies $E_{m,n}$ for the planar axis ATF at $\beta_0 = 5\%$, where

$$E_{m,n} = \int_0^{wall} \rho\left(\frac{B_{m,n}^2}{2} + \frac{P_{m,n}}{\gamma - 1}\right) d\rho \ . \tag{17}$$

The solid curves in Fig. 4 are the spectrum for a simulation in which 40 modes are retained with 34 radial grid points. The broken curves in

Fig. 4 are the differences of the $E_{m,n}$ between a 16- and 40-mode simulation. Good convergence with number of modes is evident with 16 modes. The dominant modes in the finite-β spectrum can be seen to be precisely the dominant vacuum modes (c.f. Fig. 3). A logarithmic fall off in m and n about the dominant $E_{m,n}$ occurs. This relatively rapid fall off means that the gross equilibrium properties such as equilibrium shift converge very rapidly. Figure 5 shows how the equilibrium shift converges as the number of modes retained in the equilibrium calculation increases, for the same case as Fig. 4. A very rapid convergence of the equilibrium shift is evident. The first two modes retained in Fig. 5 are the (0,0) and (1,0). The largest mode set represented in Fig. 5 corresponds to the 16-mode set, whose spectrum is shown in Fig. 4. For a flux conserving calculation, the rotational transform (ι) profile as a function of toroidal flux should be a conserved quantity. Figure 6 shows how the ι profile depends on the number of modes retained in the calculation at $\beta_0 = 5\%$. In Fig. 7 the flux surfaces are shown for the $\beta_0 = 5\%$ ATF equilibrium with 2, 7, and 16 modes retained in the calculation. All of these mode convergence results show very rapid convergence. At higher betas the spectrum broadens somewhat, but 20 modes are still sufficient to give converged results at $\beta_0 = 15\%$.

For ATF the equilibrium shift is toroidally dominated, which means that the equilibrium can be well reproduced with only two modes [the (0,0) and (1,0)]. For other devices, such as heliacs, the vacuum mode spectrum is much broader, and the toroidal and helical shifts may be comparable. The net result is that heliacs require many more harmonics (typically $\geq$25), for a well converged equilibrium. Figure 8 shows the $E_{m,n}$ spectrum ($\beta_0 = 15\%$) for a 12-field period heliac which has an ι

profile varying between 4.55 at the magnetic axis and 5.33 at the plasma edge, and a coil aspect ratio of 12. Seventy modes and 30 radial grid points were used in the calculation associated with this spectrum. The broader character of this spectrum compared to the planar axis ATF spectrum (Fig. 4) is evident. Figure 9 shows the vacuum and equilibrium flux surfaces for this case. Even though several resonant and nearly resonant harmonics are present in the calculation, no breaking or significant distortions to the flux surfaces are evident.

Another convergence property which must be studied is that of the radial mesh. Figure 10 shows how the ι profile and magnetic well profile converge with increasing radial mesh at 5% central beta for ATF (16 modes). The convergence studies shown in Fig. 10 show surprisingly good results with only seven radial mesh points; these results are, however, consistent with similar convergence studies for the Chodura-Schlüter code [9]. The 25 mesh point calculation shown in Fig. 10 required about 20 minutes of CPU time on a Cray-I computer. For rapid parameter scans of devices with toroidally dominated shifts only two modes and about 10 mesh points are required. Such calculations require only a couple of minutes of Cray-I CPU time. Convergence studies of the $E_{m,n}$ spectrum with radial mesh show that 25 radial mesh points are sufficient to resolve the dominant harmonics (those shown in Fig. 3) to an accuracy of 0.1% at $\beta = 5\%$ for the planar axis ATF. Also, 25 mesh points yield an equilibrium shift converged to 0.3% accuracy. Thus, it can be concluded that at $\beta_0 = 5\%$, the planar axis ATF requires between 20 and 30 radial mesh points for converged equilibrium solutions. At higher beta somewhat finer meshes are required - for example, at $\beta_0 = 15\%$ the errors in the $E_{m,n}$ become

approximately a factor of 1.5 worse than the equivalent errors for the $\beta_0 = 5\%$ case. Figure 11 shows how the $\beta_0 = 5\%$ ATF equilibrium flux surfaces converge for increasingly fine meshes.

The convergence of the solutions with the time-step size used in time advancing $\vec{B}$ and P has also been studied. Typically, a timestep 2 or 3 times smaller than that permitted by numerical stability considerations is used. The convergence of the solution with timestep size is regularly checked by reducing the timestep and repeating the calculation.

The most important convergence is the convergence toward a solution of the equilibrium equations. The equilibrium iteration scheme makes use of a volume average of the force $[\langle\vec{F}^2\rangle]$ which provides a sensitive measure of the equilibrium convergence. Figure 12 shows how $\langle\vec{F}^2\rangle$ decreases as a function of iteration during a $\beta_0 = 5\%$, ATF equilibrium calculation. Also shown in Fig. 12 is the history of equilibrium shift during the calculation. The conjugate gradient iteration scheme gives a rapid logarithmic reduction of $\langle\vec{F}^2\rangle$ and convergence of the shift. No attempt has been made to examine alternate convergence schemes. The fact that the $\langle\vec{F}^2\rangle$ saturates at some final value is due to the numerical resistivity arising from radial differencing errors. The final value of $\langle\vec{F}^2\rangle$ scales approximately as $(\Delta\rho)^{-2}$, where $\Delta\rho$ is the radial mesh size.

Another measure of the equilibrium convergence is given by the requirement that for an exact equilibrium $\vec{B} \cdot \vec{\nabla}P = 0$. To measure how well the NEAR equilibria satisfy this relation the variance of the pressure on a magnetic surface is calculated as a diagnostic. Here the variance is defined as

$$\bar{P} = \frac{[(\int P d\ell)^2 - \int P^2 d\ell]^{1/2}}{\int P d\ell} \tag{18}$$

where the path of the integral is along a magnetic field line and the asymptotic value of $\bar{P}$ is obtained by following the field line for many turns. Figure 13 shows $\bar{P}$ as function of radius for a $\beta_0 = 5\%$, 16-mode, 34 radial mesh point equilibrium. The error ($\bar{P}$) is almost entirely due to radial differencing errors arising during the equilibrium calculation and also during the evaluation of $\bar{P}$. This error scales as $(\Delta\rho)^{-2}$ but is relatively insensitive to the number of modes retained in the equilibrium calculation. Although this diagnostic provides a further validation of the code, the gross equilibrium properties, such as shift, magnetic well, and ι profile provide much better measures of the necessary resolution for convergence.

The results of calculations with the NEAR code have been benchmarked against various other codes. Some of these comparisons are given in Ref. [10]. Here the NEAR equilibrium calculations for ATF will be compared with results from the Chodura-Schlüter code. Figure 14 shows a comparison of the equilibrium flux surfaces ($\beta_0 = 5\%$) between the two equilibrium codes. To make this comparison more quantitative, the equilibrium shift and magnetic well profile computed with the Chodura-Schlüter code and NEAR are compared in Figs. 15 and 16, respectively. The good agreement between the NEAR code and the other codes provides a valuable validation of the NEAR code. Finally in Fig. 17, the magnetic well depth as a function of β_0 computed with the NEAR code and Chodura-Schlüter code are compared. At low beta ($\lesssim 7\%$) the codes agree well. At higher betas, where the resolution of the Chodura-Schlüter code is less adequate, the agreement deteriorates.

5. CONCLUSIONS

Details of a 3-D stellarator equilibrium code (NEAR) have been given. This code employs the vacuum flux coordinates described by Boozer, as an Eulerian frame of reference. These coordinates have been shown to provide an efficient representation of the complex stellarator geometry. The NEAR code solves the equilibrium equations in these coordinates, subject to the constraints of flux and mass conservation. The code relaxes the equations to an equilibrium by an energy minimization technique. A Fourier series representation is used in the poloidal (θ) and toroidal (ϕ) directions, and a finite difference representation is used in the radial direction (ρ). A first order explicit scheme is used to time advance the magnetic field and pressure.

Equilibrium convergence studies are presented for the planar axis ATF. The vacuum mode spectrum is shown to provide a good guide of the relative importance of a given mode in the equilibrium calculations. Convergence studies in the number of radial mesh points show that between 20 and 30 points are sufficient. Also the equilibrium properties of a 12-field period heliac have been briefly examined. It is found that heliacs have broader spectra and require more modes for converged results than the planar axis ATF.

The NEAR code has been benchmarked against existing stellarator equilibrium codes. Comparisons of flux surfaces, equilibrium shift and magnetic well profiles with the Chodura-Schlüter code show good agreement – thus further validating the code.

ACKNOWLEDGMENTS

We should like to acknowledge many useful discussions with members of the ATF group. In particular, the contributions of J. H. Harris and J. L. Cantrell to the heliac studies are gratefully acknowledged. We should also like to thank the Max-Planck Institut für Plasmaphysik and, in particular, Dr. R. Chodura and Dr. A. Schlüter for providing us with a copy of their equilibrium code.

REFERENCES

[1] J. M. Greene and J. L. Johnson, Phys. Fluids 4, (1961) 875.

[2] D. Lortz and J. Nührenberg, Naturforsch 31a, 1277; Nucl. Fusion 17, (1977) 125.

[3] R. Chodura and A. Schlüter, J. Comput. Phys. 41, (1981) 68.

[4] F. Bauer, O. Betancourt, and P. Garabedian, A Computational Method in Plasma Physics, Springer-Verlag, New York, 1978.

[5] J. F. Lyon, B. A. Carreras, J. H. Harris, J. A. Rome, R. A. Dory, L. Garcia, T. C. Hender, S. P. Hirshman, T. C. Jernigan, J. Sheffield, L. A. Charlton, R. H. Fowler, H. R. Hicks, J. A. Holmes, V. E. Lynch, B. F. Masden, D. L. Goodman, and S. A. Hokin, Oak Ridge Natl. Lab. Report ORNL/TM-8496, 1983.

[6] A. H. Boozer, T. K. Chu, R. L. Dewar, H. P. Furth, J. A. Goree, J. L. Johnson, R. M. Kulsrud, D. A. Monticello, G. Kuo-Petravic, G. V. Sheffield, S. Yoshikawa, and O. Betancourt, in Plasma Physics and Controlled Nuclear Fusion Research Vol. 3, p. 129, IAEA, Vienna, 1983.

[7] A. H. Boozer, Phys. Fluids 25, (1982) 520.

[8] G. Kuo-Petravic, A. H. Boozer, J. A. Rome, and R. H. Fowler, J. Comp. Phys. 51, (1983) 261.

[9] L. Garcia, B. A. Carreras, J. H. Harris, H. R. Hicks, and V. E. Lynch, Nucl. Fusion 24, (1984) 115.

[10] B. A. Carreras, H. R. Hicks, J. A. Holmes, V. E. Lynch, L. Garcia, J. H. Harris, T. C. Hender, and B. F. Masden, Phys. Fluids 26, (1983) 3569.

Appendix: Finite Difference Form of the NEAR Equations

The following notation will be used in this Appendix - a bracket around a variable denotes the (m,n) Fourier component of that variable ($[A] \equiv A_{m,n}$), superscripts denote iteration level, and subscripts indicate radial mesh position.

With this notation the components of the current ($\vec{J}$) in finite difference form are

$$[J_\rho]^n_{i+1/2} = \frac{-m}{r_i}[B_\phi]^n_{i+1/2} + n[B_\theta]^n_{i+1/2},$$

$$[J_\theta]^n_i = n[B_\rho]^n_i - \frac{[B_\phi]^n_{i+1/2} - [B_\phi]^n_{i-1/2}}{\Delta\rho},$$

and

$$[J_\phi]^n_i = \frac{\rho_{i+1/2}[B_\theta]^n_{i+1/2} - \rho_{i-1/2}[B_\theta]^n_{i-1/2}}{\rho_i \Delta\rho} - \frac{m}{\rho_i}[B_\rho]^n_i,$$

where $\Delta\rho$ is the radial mesh step and the subscript i+1/2 denotes a point of the intermediate mesh halfway between ρ_i and ρ_{i+1} [many of the variables are stored on this mesh as explained in Section 3(b)].

In finite difference form, the components of the equilibrium equation [Eq. (6)] are

$$[F_\rho]^{n+1}_i = [B^\phi_i J^\theta_i]^n - [B^\theta_i J^\phi_i]^n - \frac{[P]^n_{i+1/2} - [P]^n_{i-1/2}}{\Delta\rho},$$

$$[F_\theta]^{n+1}_{i+1/2} = \frac{[B^\rho_i J^\phi_i]^n + [B^\rho_{i+1} J^\phi_{i+1}]^n}{2} - [B^\phi_{i+1/2} J^\rho_{i+1/2}]^n + \frac{m[P]^n_{i+1/2}}{\rho_i} ,$$

and

$$[F_\phi]^{n+1}_{i+1/2} = [B^\theta_{i+1/2} J^\rho_{i+1/2}]^n - \frac{[B^\rho_i J^\theta_i]^n + [B^\rho_{i+1} J^\theta_{i+1}]^n}{2} + n[P]^n_{i+1/2} .$$

In finite difference form the flux conservation equation [Eq. (8)] is

$$\frac{[B^\theta/D_v]^{n+1}_{i+1/2} - [B^\theta/D_v]^n_{i+1/2}}{\Delta t} = n[v^\theta_{i+1/2}(B^\phi/D_v)_{i+1/2} - v^\phi_{i+1/2}(B^\theta/D_v)_{i+1/2}]^n$$

$$- \frac{[V^\rho_{i+1}(B^\theta/D_v)_{i+1} - V^\theta_{i+1}(B^\rho/D_v)_{i+1} - V^\rho_i(B^\theta/D_v)_i + V^\theta_i(B^\rho/D_v)_i]^n}{\Delta\rho}$$

and

$$\frac{[B^\phi/D_v]^{n+1}_{i+1/2} - [B^\phi/D_v]^n_{i+1/2}}{\Delta t} = \frac{-m}{\rho_{i+1/2}}[V^\theta_{i+1/2}\ (B^\phi/D_v)_{i+1/2} - V^\phi_{i+1/2}\ (B^\theta/D_v)_{i+1/2}]^n$$

$$+ \frac{\rho_{i+1}[V^\phi_{i+1}(B^\rho/D_v)_{i+1} - V^\rho_{i+1}(B^\phi/D_v)_{i+1}]^n - \rho_i[V^\phi_i(B^\rho/D_v)_i - V^\rho_i(B^\phi/D_v)_i]^n}{\rho_{i+1/2}\ \Delta\rho} ,$$

where Δt is the timestep. From $\nabla \cdot \vec{B} = 0$ an equation for (B^ρ/D_v) is given:

$$[B^\rho/D_v]^n_i = \left(\rho_{i+1}[B^\rho/D_v]^n_{i+1} - \Delta\rho\ m[B^\phi/D_v]^n_{i+1/2} - \Delta\rho\ \rho_{i+1/2}{}^n[B\phi/D_v]^n_{i+1/2}\right)\rho_i{}^{-1} .$$

This equation, together with the wall boundary condition $[B^\rho/D_v] = 0$,

is sufficient to iteratively determine (B^{ρ}/D_v). Finally, the pressure equation [Eq. (9)] becomes, in finite difference form,

$$\frac{[P]^{n+1}_{i+1/2} - [P]^{n}_{i+1/2}}{\Delta t} = -\left[V^{\rho}_{i+1/2}\frac{(P_{i+1} - P_i)}{\Delta\rho}\right]^n - \frac{1}{\rho_{i+1/2}}\left[V^{\theta}_{i+1/2}\frac{\partial P_{i+1/2}}{\partial\theta}\right]^n$$

$$- \left[V^{\phi}_{i+1/2}\frac{\partial P_{i+1/2}}{\partial\phi}\right]^n - \gamma\left[P_{i+1/2}(\nabla\cdot\vec{V})_{i+1/2}\right]^n ,$$

where $\nabla\cdot\vec{V}$, in finite difference form, is

$$\left[\nabla\cdot\vec{V}\right]^n_{i+1/2} = \frac{1}{\rho_{i+1/2}}\left[(D_v)_{i+1/2}\Delta\rho^{-1}\left(\rho_{i+1}(V^{\rho}/D_v)_{i+1} - \rho_i(V^{\rho}/D_v)_i\right)\right]^n$$

$$+ \frac{1}{\rho_{i+1/2}}\left[(D_v)_{i+1/2}\frac{\partial}{\partial\theta}(V^{\theta}/D_v)_{i+1/2}\right]^n + \left[(D_v)_{i+1/2}\frac{\partial}{\partial\phi}(V^{\phi}/D_v)_{i+1/2}\right]^n .$$

Many of the above equations implicitly involve Fourier convolutions. For example, the last term of the last equation requires the convolution of V^{ϕ} and $1/D_v$.

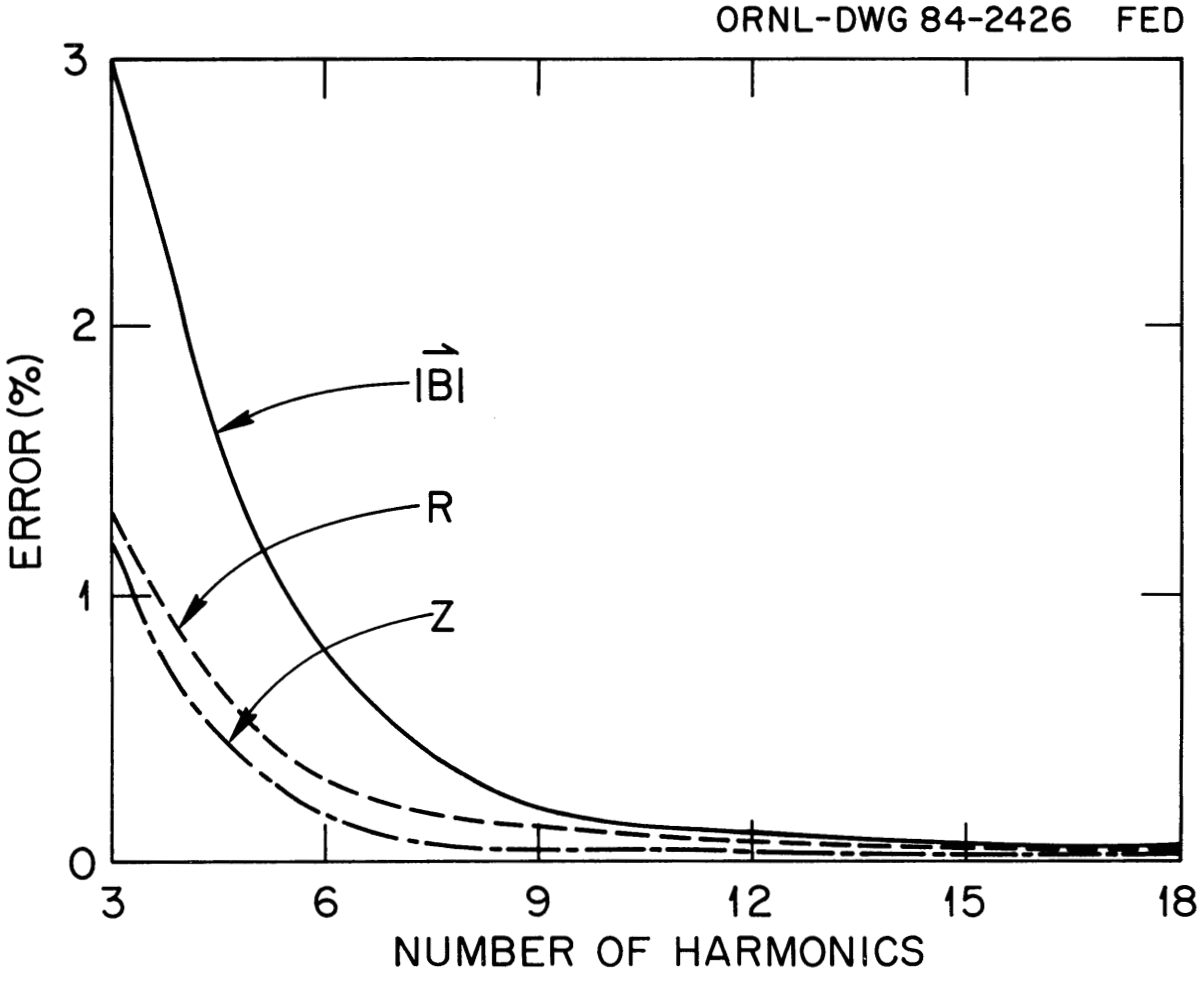

Fig. 1. Error in representing R, Z, and $|\vec{B}|$ as Fourier Series with a given number of terms.

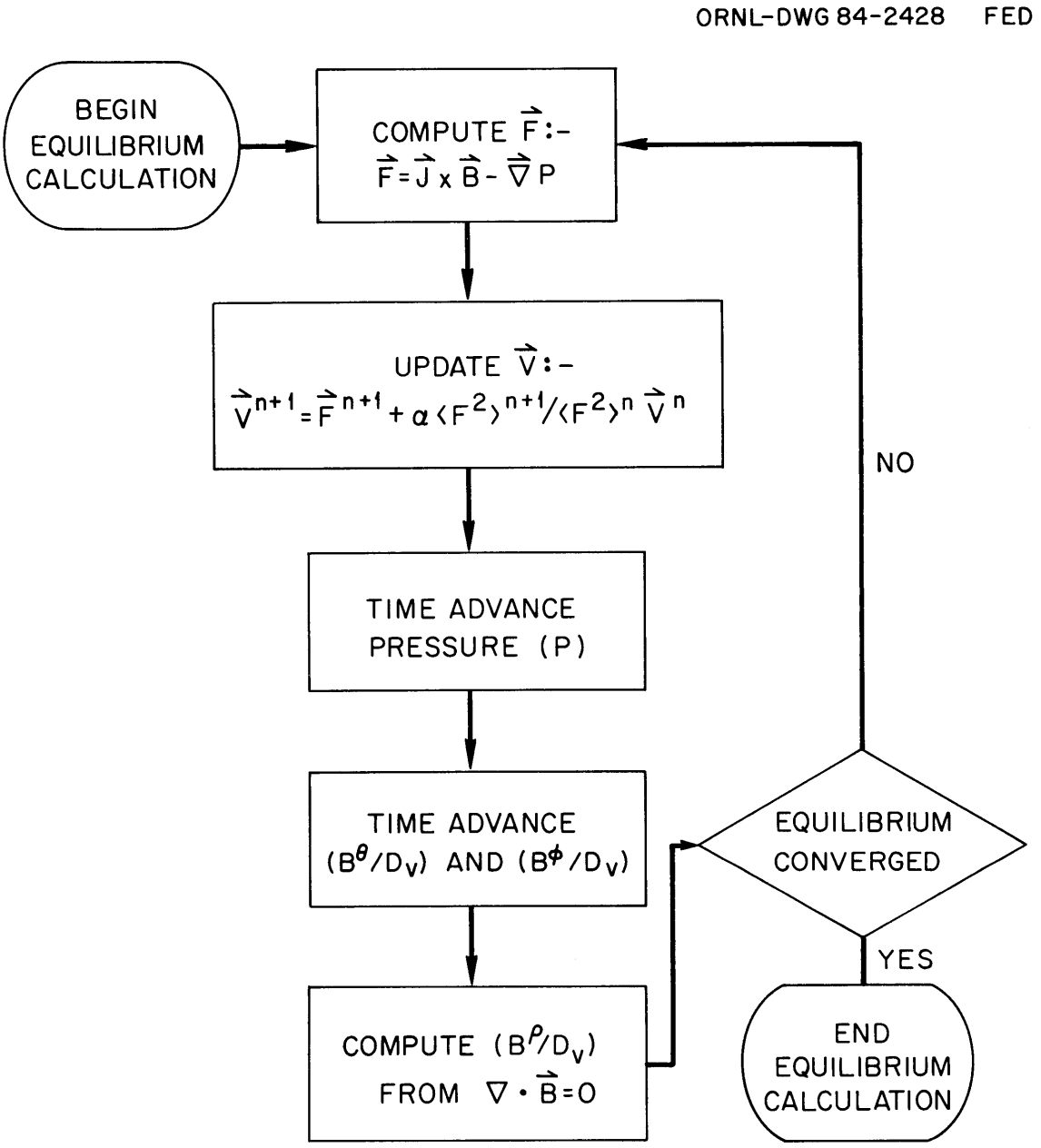

Fig. 2. Flow diagram of the NEAR algorithm.

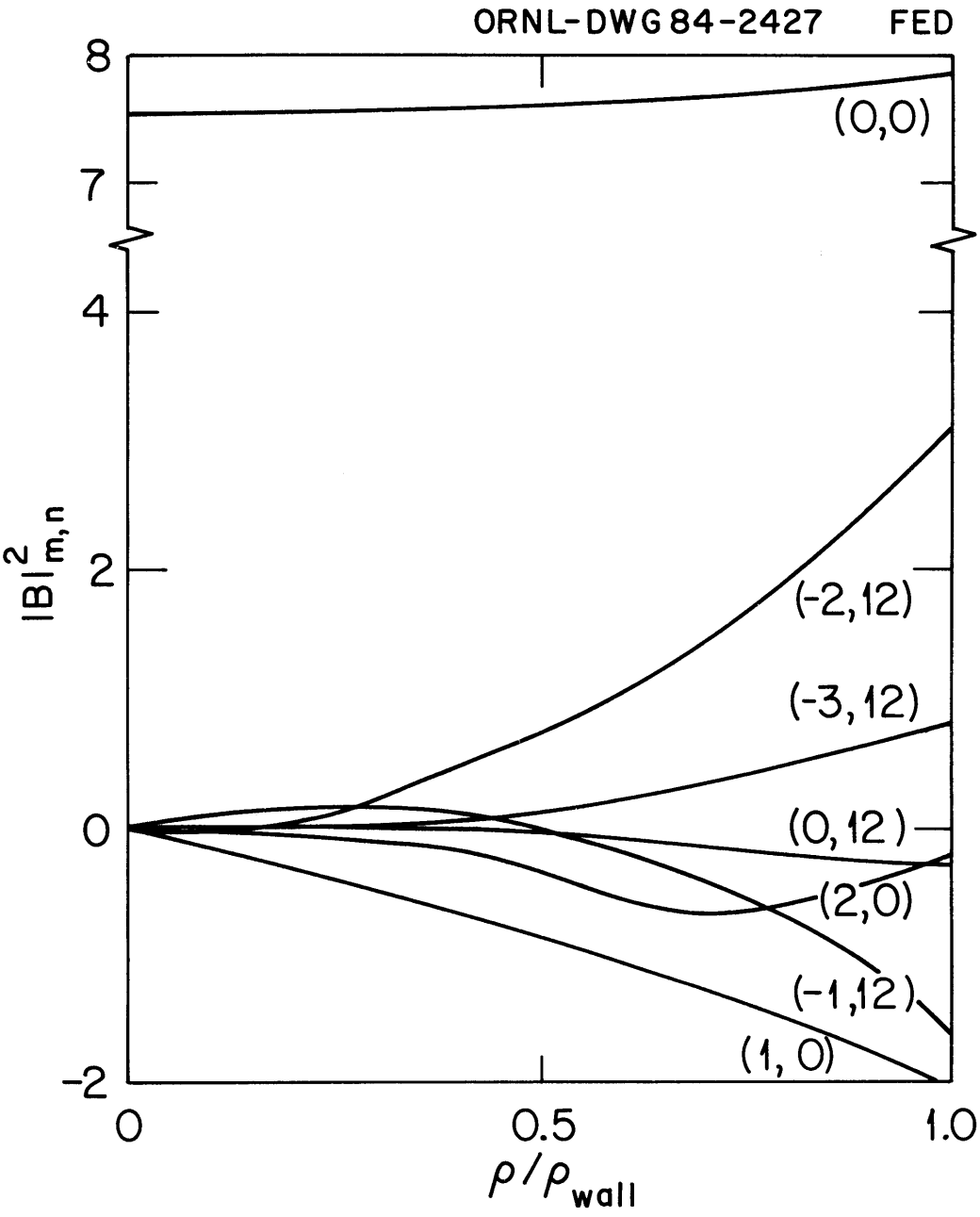

Fig. 3. Dominant $B^2_{m,n}$ in the vacuum representation of the planar axis ATF.

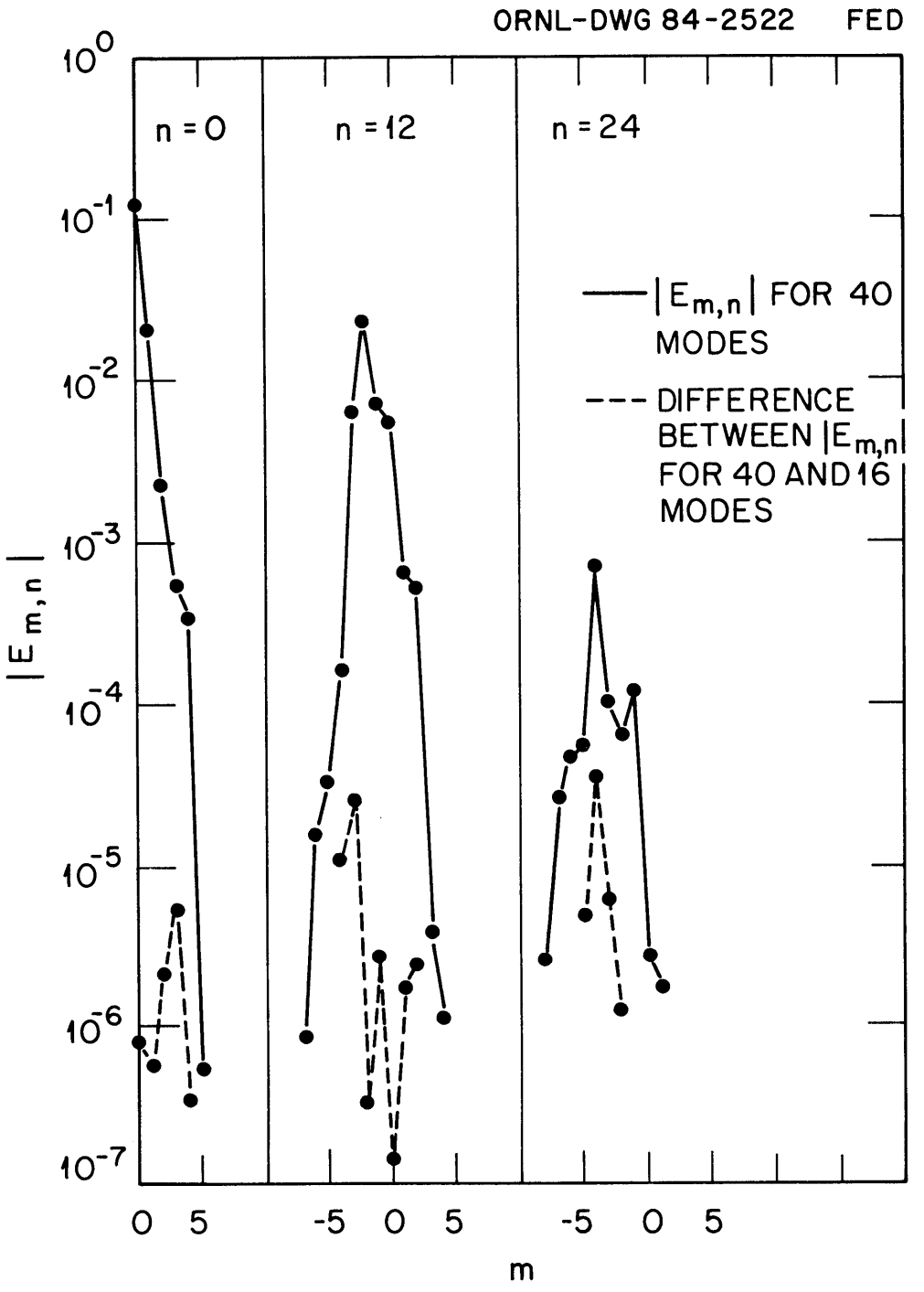

Fig. 4. $E_{m,n}$ spectrum for $\beta_0 = 5\%$ planar axis ATF. Solid curve is for a 40-mode case and the broken curve is the difference between the $E_{m,n}$ for 40 and 16 modes.

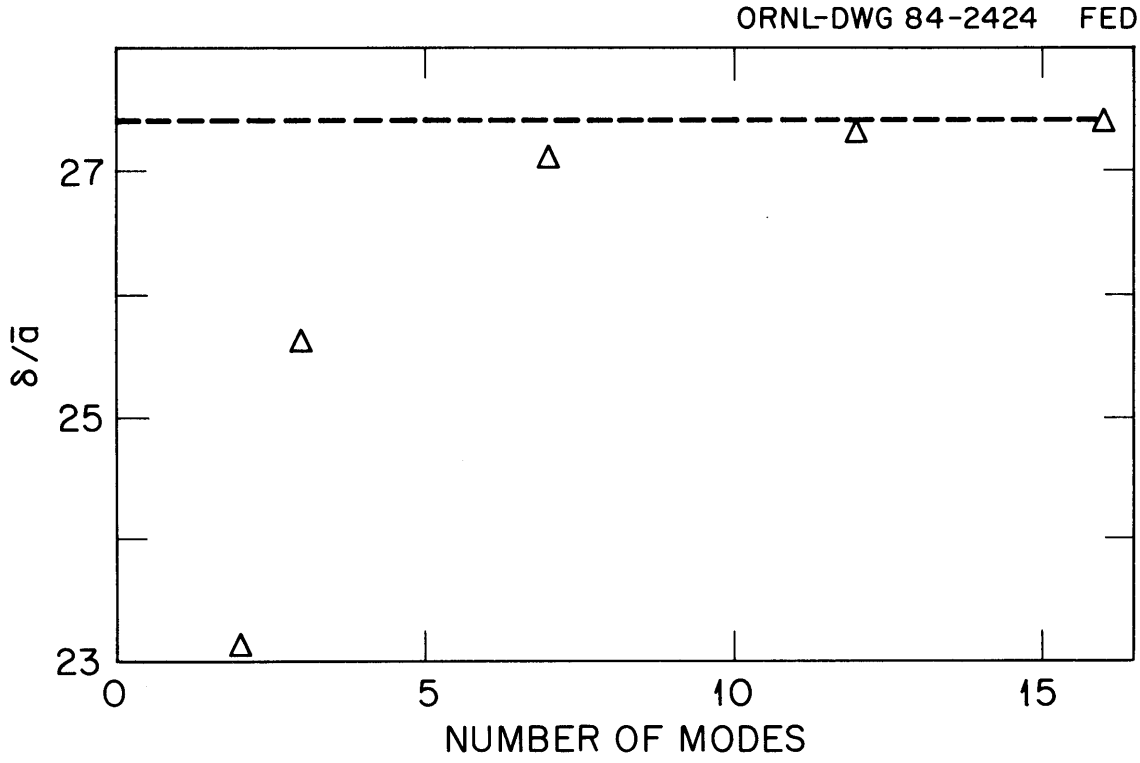

Fig. 5. Convergence of equilibrium shift with number of modes for $\beta_0 = 5\%$ planar axis ATF.

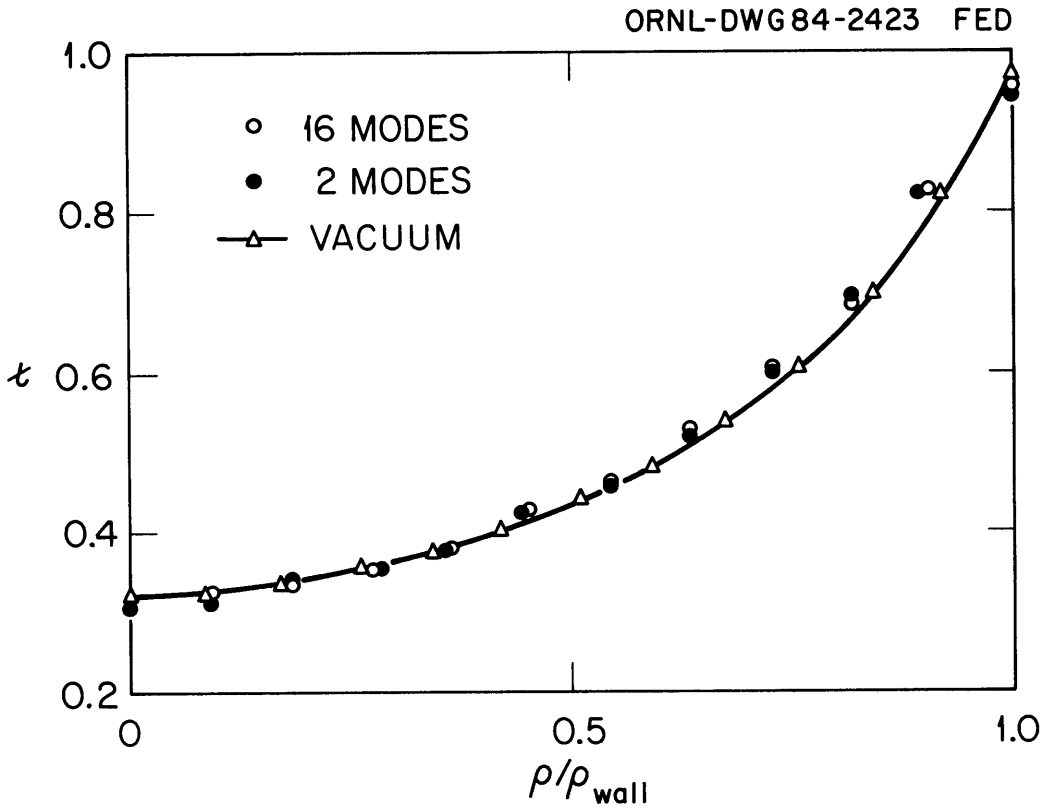

Fig. 6. Dependence of ι profile on number of modes for β_0 = 5% planar axis ATF. (Vacuum ι profile is shown for reference.)

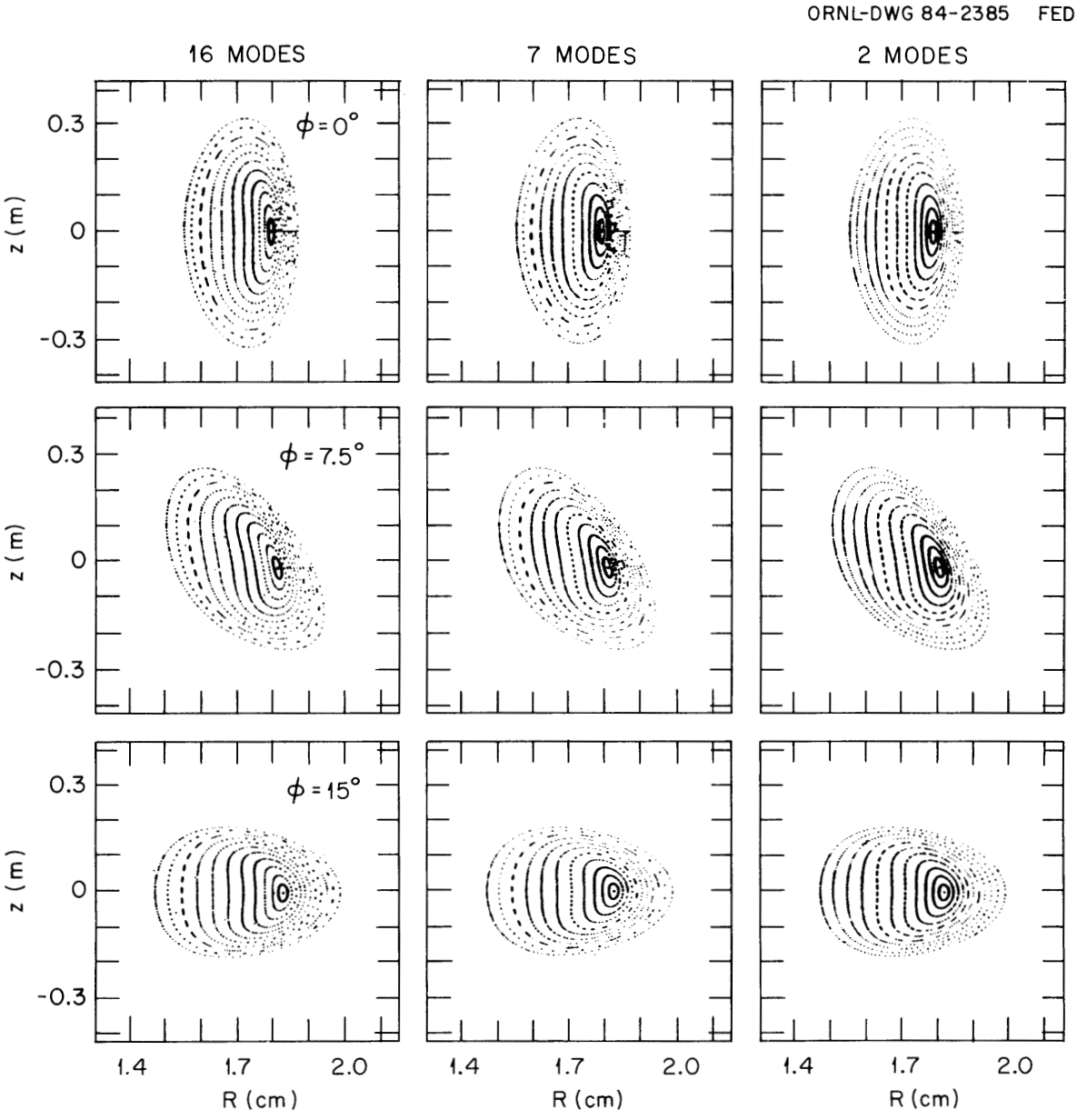

Fig. 7. Convergence of flux surfaces with number of modes for β_0 = 5% planar axis ATF.

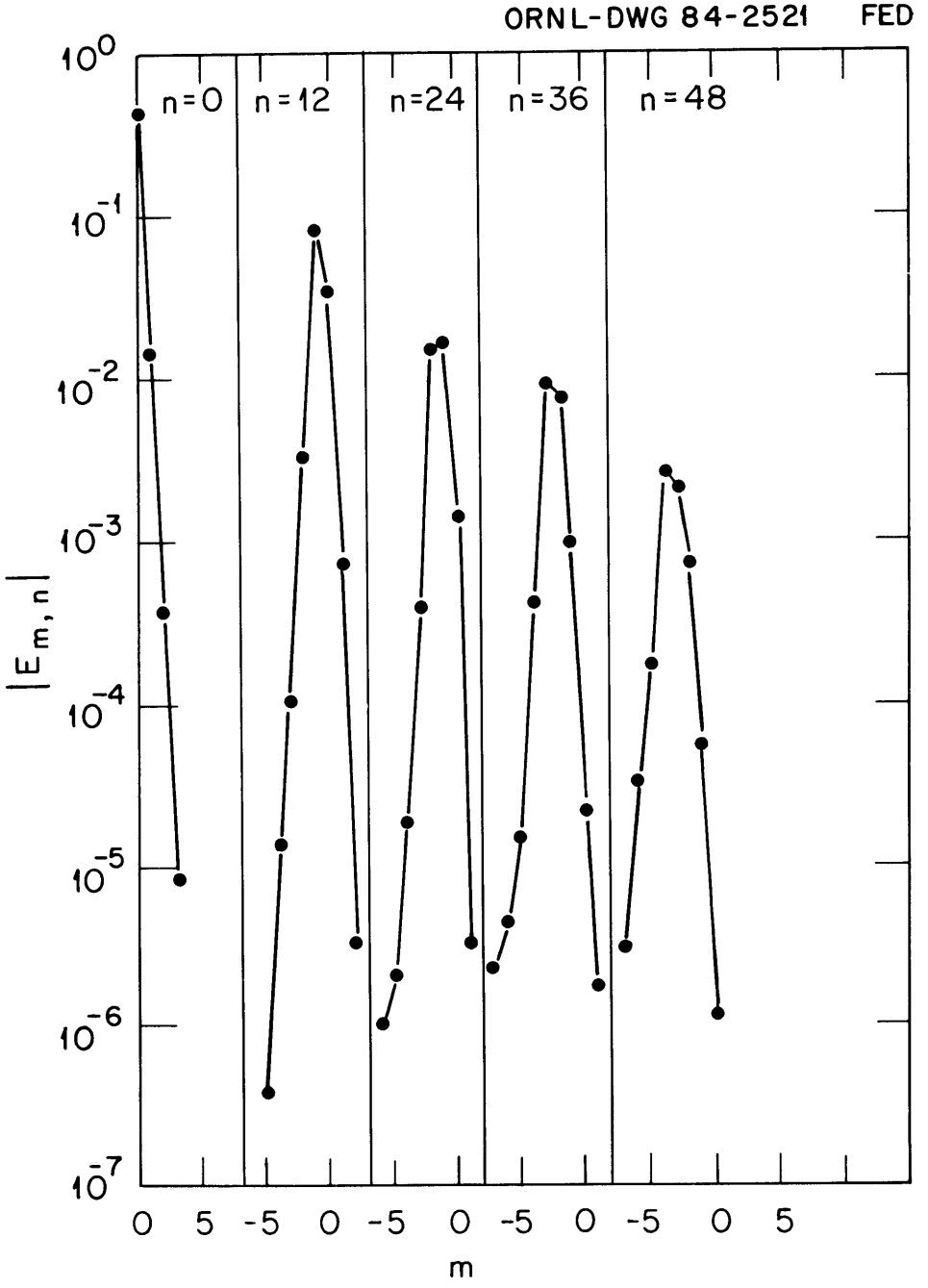

Fig. 8. $E_{m,n}$ spectrum for a 70-mode simulation of a 12-field period heliac (β_0 = 15%).

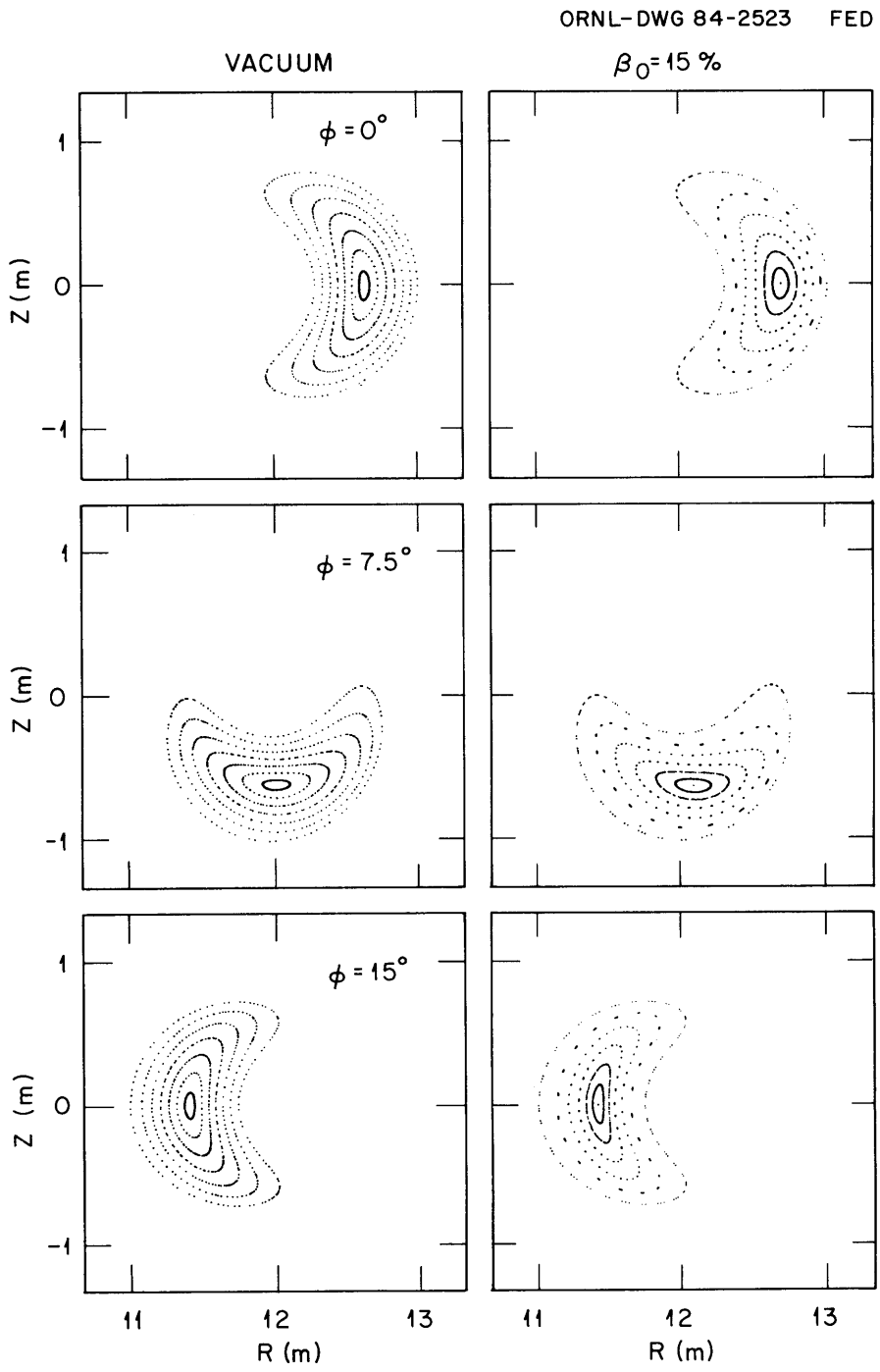

Fig. 9. Flux surfaces for the 12-field period heliac whose spectrum is shown in Fig. 8.

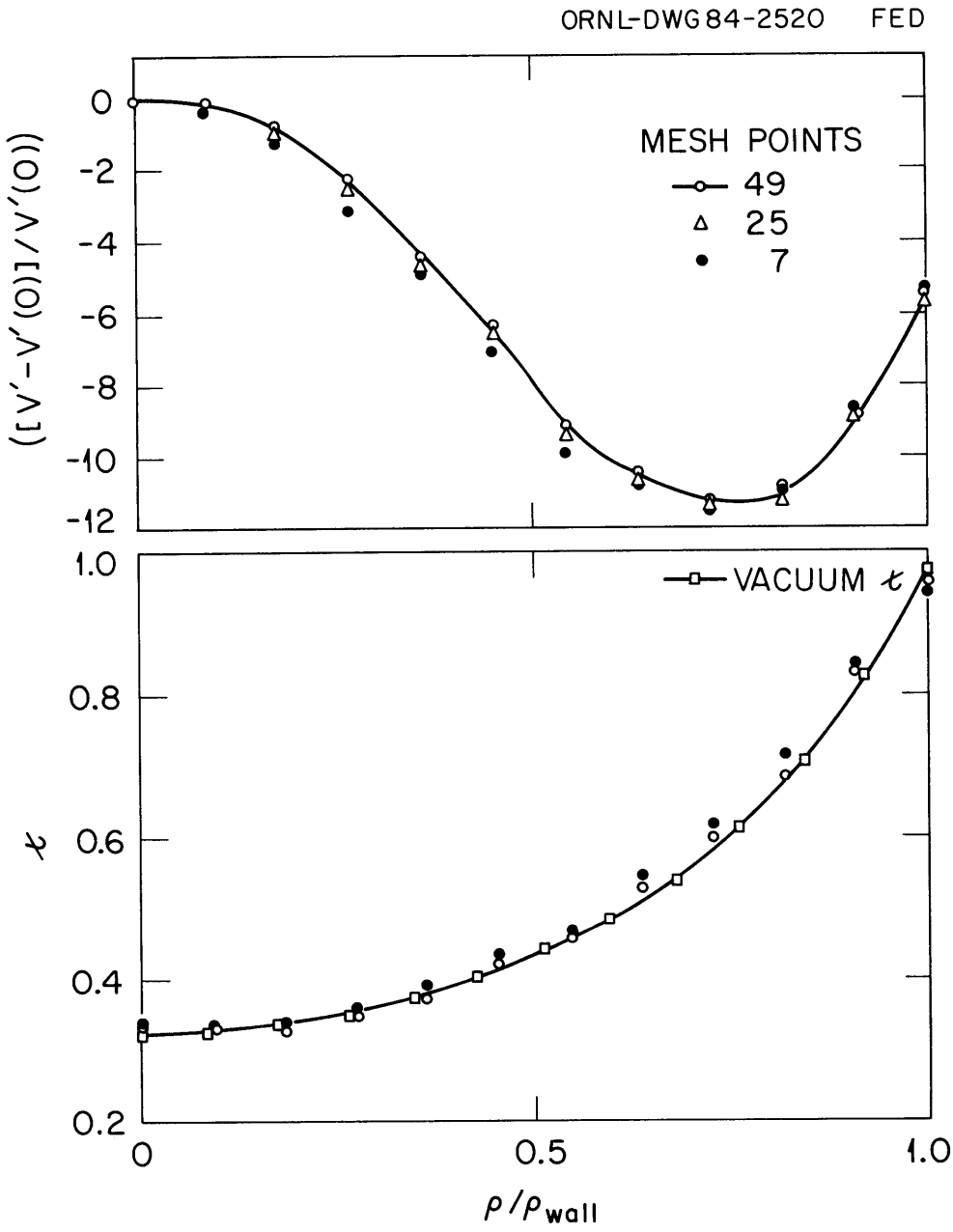

Fig. 10. Dependence of magnetic well (upper plot) and ι profile (lower plot) on number of radial grid points for the $\beta_0 = 5\%$ planar axis ATF.

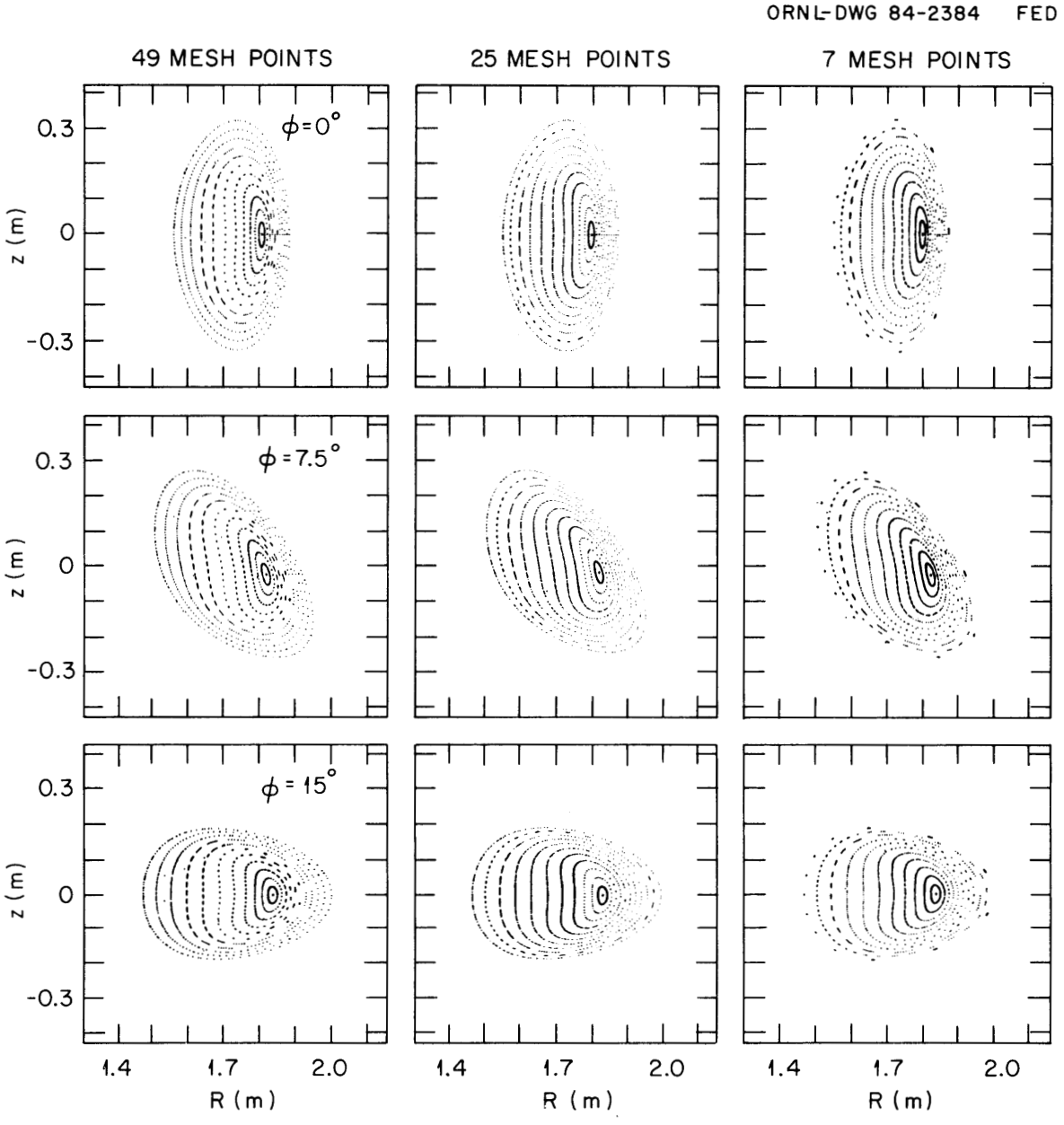

Fig. 11. Convergence of flux surfaces with number of radial grid points for the $\beta_0 = 5\%$ planar axis ATF.

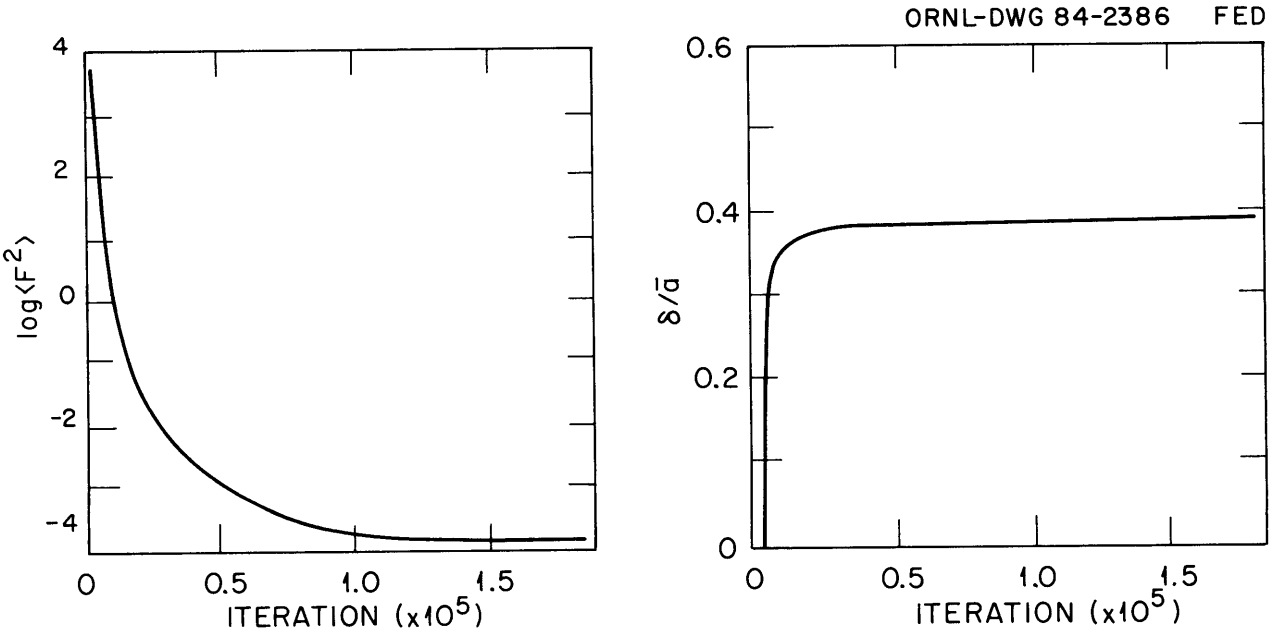

Fig. 12. Residual force $\langle \vec{F}^2 \rangle$ and equilibrium shift $(\delta/\bar{a})$ for a $\beta_0 = 5\%$ planar axis ATF calculation.

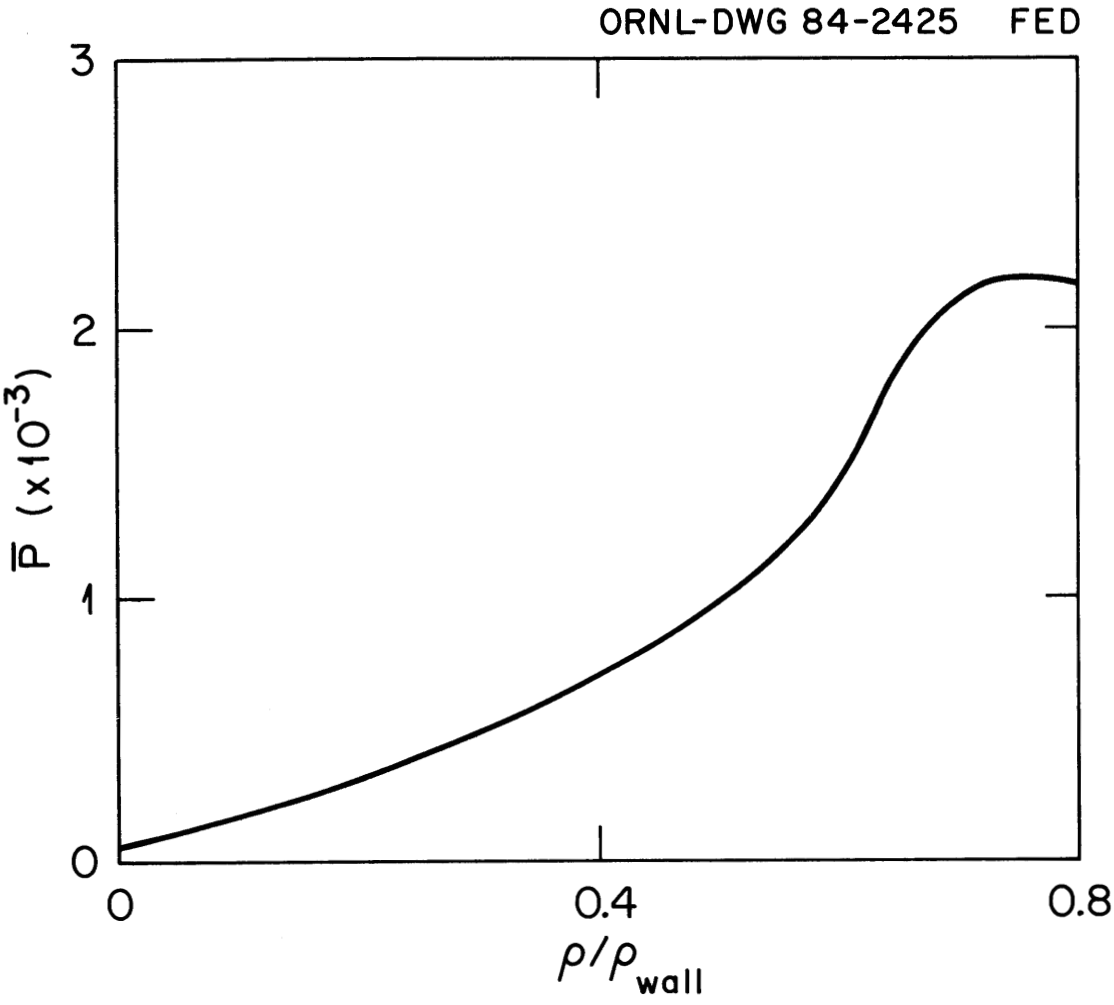

Fig. 13. Variance of the pressure ($\bar{P}$) as a function of radius for planar axis ATF (parameters given in the text).

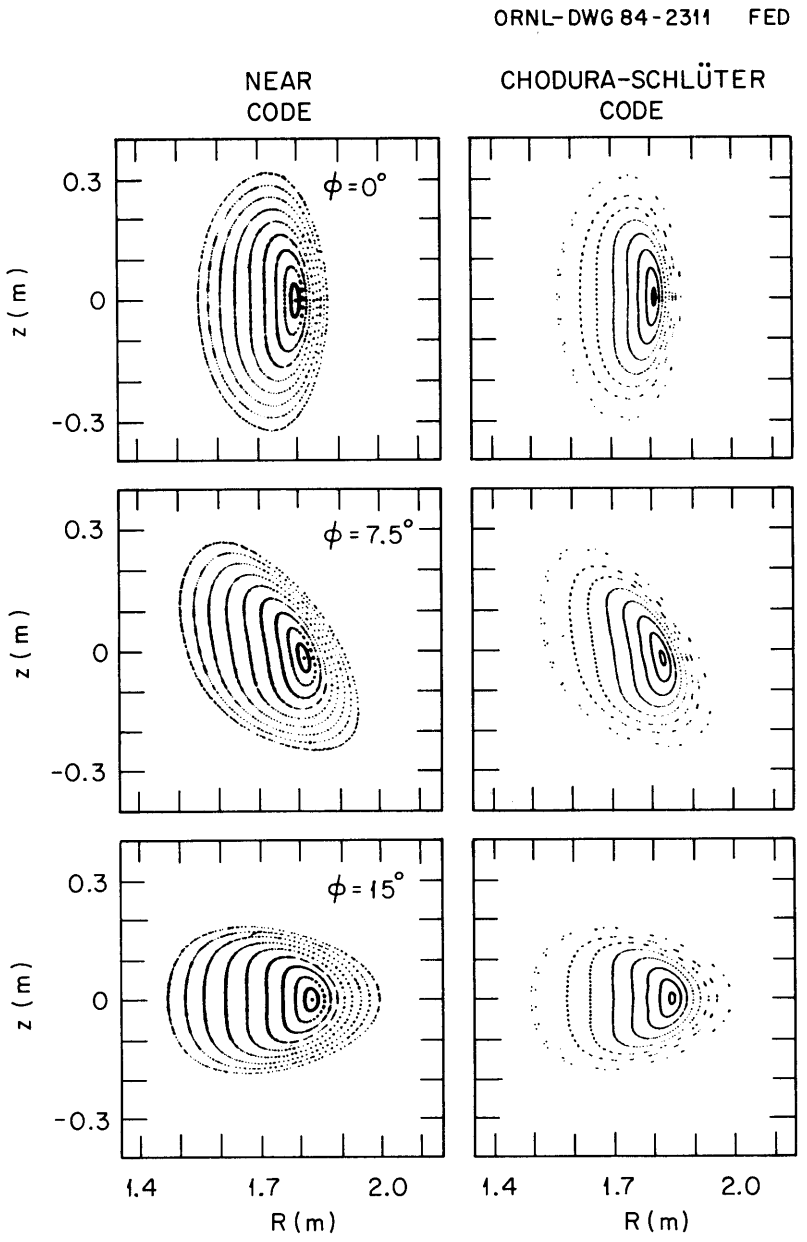

Fig. 14. Comparison of the equilibrium flux surfaces computed with NEAR and Chodura-Schlüter code for the planar axis ATF (β_0 = 5%).

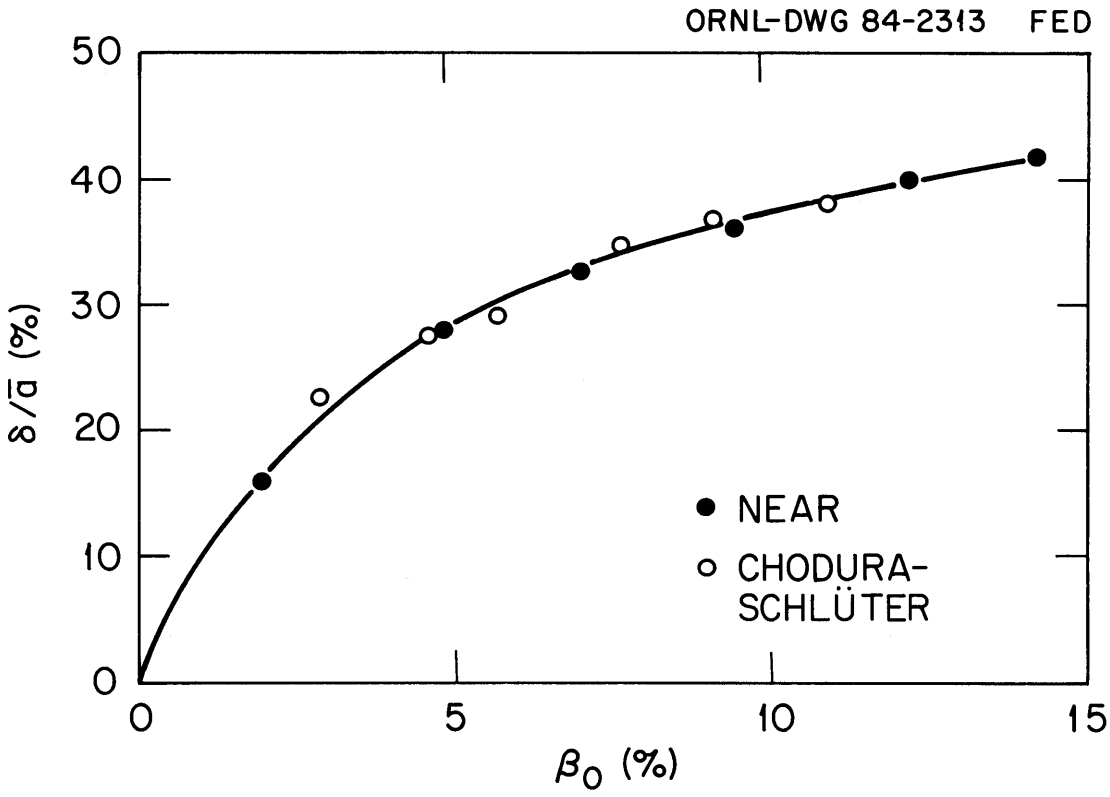

Fig. 15. Comparison of equilibrium shift computed with NEAR and the Chodura-Schlüter code for the planar axis ATF.

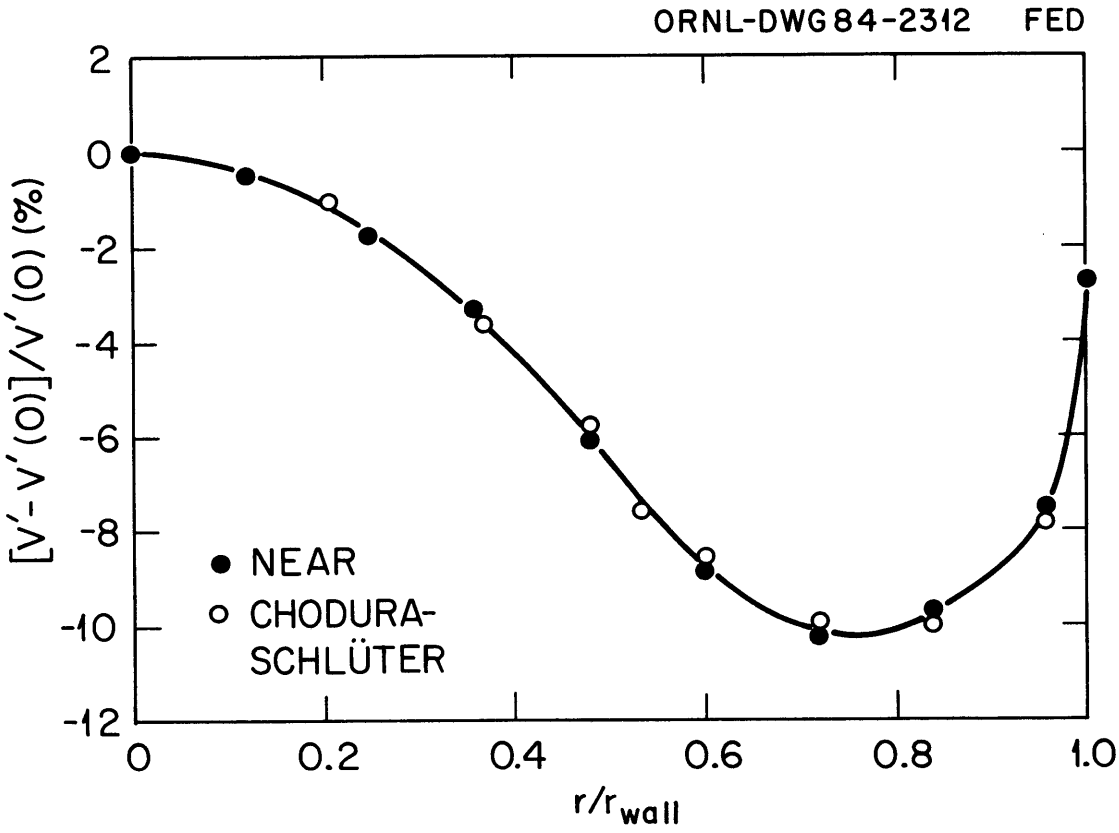

Fig. 16. Comparison of the magnetic well profile computed with NEAR and Chodura-Schlüter code for the equilibrium shown in Fig. 14 (β_0 = 5%).

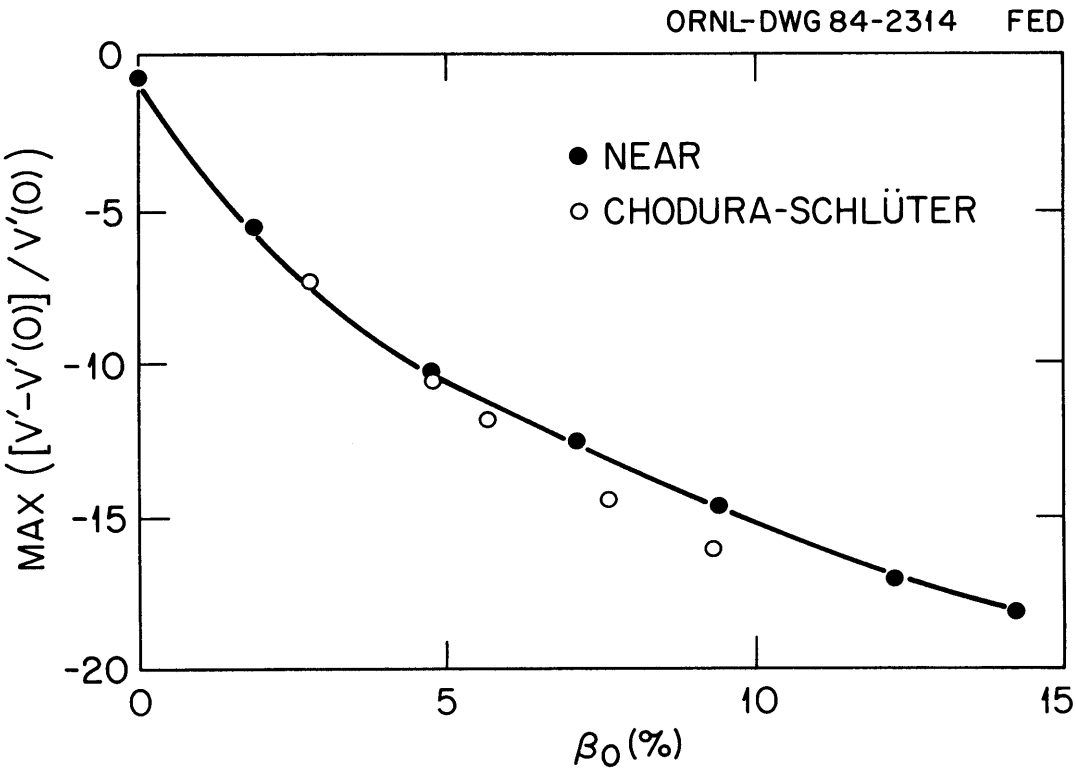

Fig. 17. Comparison of magnetic well depth as a function of β_0 between NEAR and the Chodura-Schlüter code for the planar axis ATF.

ORNL/TM-9239
Dist. Category UC-20

INTERNAL DISTRIBUTION

1. B. A. Carreras
2. R. A. Dory
3. L. Garcia
4. J. H. Harris
5–9. T. C. Hender
10. H. R. Hicks
11. J. A. Holmes
12. J. K. Johnson
13. V. E. Lynch
14. J. A. Rome
15. D. J. Sigmar
16–17. Laboratory Records Department
18. Laboratory Records, ORNL-RC
19. Document Reference Section
20. Central Research Library
21. Fusion Energy Division Library
22. Fusion Energy Division Reports Office
23. ORNL Patent Office

EXTERNAL DISTRIBUTION

24. D. C. Robinson, Culham Laboratory, Abingdon, Oxfordshire, OX143DB, England
25. D. Monticello, Princeton Plasma Physics Laboratory, P.O. Box 451, Princeton, NJ 08544
26. B. McNamara, Lawrence Livermore National Laboratory, Box 5511, University of California, Livermore, CA 94550
27. D. Dobrott, Science Applications, Inc., P.O. Box 2351, La Jolla, CA 92038
28. P. Garabedian, Courant Institute, New York University, 251 Mercer Street, New York, NY 10012
29. Office of the Assistant Manager for Energy Research and Development, Department of Energy, Oak Ridge Operations, Box E, Oak Ridge, TN 37831
30. J. D. Callen, Department of Nuclear Engineering, University of Wisconsin, Madison, WI 53706
31. R. W. Conn, Department of Chemical, Nuclear, and Thermal Engineering, University of California, Los Angeles, CA 90024
32. S. O. Dean, Director, Fusion Energy Development, Science Applications, Inc., 2 Professional Drive, Gaithersburg, MD 20760
33. H. K. Forsen, Bechtel Group, Inc., Research Engineering, P.O. Box 3965, San Francisco, CA 94105
34. R. W. Gould, Department of Applied Physics, California Institute of Technology, Pasadena, CA 91125
35. D. G. McAlees, Exxon Nuclear Company, Inc., 777 106th Avenue NE, Bellevue, WA 98009
36. P. J. Reardon, Princeton Plasma Physics Laboratory, P.O. Box 451, Princeton, NJ 08544
37. W. M. Stacey, Jr., School of Nuclear Engineering, Georgia Institute of Technology, Atlanta, GA 30332
38. G. A. Eliseev, I. V. Kurchatov Institute of Atomic Energy, P.O. Box 3402, 123182 Moscow, U.S.S.R.
39. V. A. Glukhikh, Scientific-Research Institute of Electro-Physical Apparatus, 188631 Leningrad, U.S.S.R.

40. I. Spighel, Lebedev Physical Institute, Leninsky Prospect 53, 117924 Moscow, U.S.S.R.
41. D. D. Ryutov, Institute of Nuclear Physics, Siberian Branch of the Academy of Sciences of the U.S.S.R., Sovetskaya St. 5, 630090 Novosibirsk, U.S.S.R.
42. V. T. Tolok, Kharkov Physical-Technical Institute, Academical St. 1, 310108 Kharkov, U.S.S.R.
43. R. Varma, Physical Research Laboratory, Navrangpura, Ahmedabad, India
44. Bibliothek, Max-Planck Institut fur Plasmaphysik, D-8046 Garching bei Munchen, Federal Republic of Germany
45. Bibliothek, Institut fur Plasmaphysik, KFA, Postfach 1913, D-5170 Julich, Federal Republic of Germany
46. Bibliotheque, Centre de Recherches en Physique des Plasmas, 21 Avenue des Bain, 1007 Lausanne, Switzerland
47. Bibliotheque, Service du Confinement des Plasmas, CEA, B.P. 6, 92 Fontenay-aux-Roses (Seine), France
48. Documentation S.I.G.N., Departement de la Physique du Plasma et de la Fusion Controlee, Centre d'Etudes Nucleaires, B.P. No. 85, Centre du Tri, 38041 Cedex, Grenoble, France
49. Library, Culham Laboratory, UKAEA, Abingdon, Oxfordshire, OX14 3DB, England
50. Library, FOM Instituut voor Plasma-Fysica, Rijnhuizen, Jutphaas, The Netherlands
51. Library, Institute of Physics, Academia Sinica, Beijing, Peoples Republic of China
52. Library, Institute of Plasma Physics, Nagoya University, Nagoya 64, Japan
53. Library, International Centre for Theoretical Physics, Trieste, Italy
54. Library, Laboratorio Gas Ionizzati, Frascati, Italy
55. Library, Plasma Physics Laboratory, Kyoto University, Gokasho Uji, Kyoto, Japan
56. Plasma Research Laboratory, Australian National University, P.O. Box 4, Canberra, A.C.T. 2000, Australia
57. Thermonuclear Library, Japan Atomic Energy Research Institute, Tokai, Naka, Ibaraki, Japan

58–164. Given distribution as shown in TID-4500, Magnetic Fusion Energy (Category Distribution UC-20)